

Effect of Interfacial Molecular Orientation on Power Conversion Efficiency of Perovskite Solar Cells

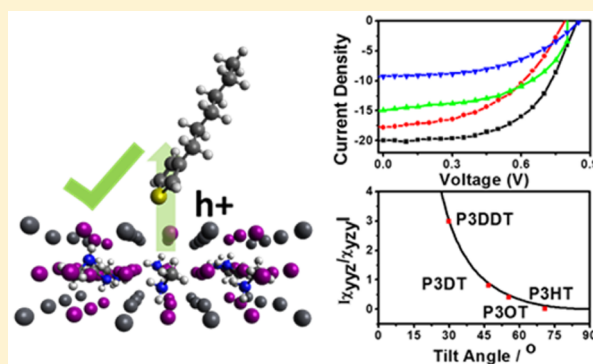
Minyu Xiao,[†] Suneel Joglekar,[‡] Xiaoxian Zhang,[§] Joshua Jasensky,[†] Jialiu Ma,[†] Qingyu Cui,[‡] L. Jay Guo,^{*,‡} and Zhan Chen^{*,†}

[†]Department of Chemistry and [‡]Department of Electrical Engineering and Computer Science, University of Michigan, Ann Arbor, Michigan 48109, United States

[§]CAS Key laboratory of Standardization and Measurement for Nanotechnology, Chinese Academy of Sciences Center for Excellence in Nanoscience, National Center for Nanoscience and Technology, Beijing 100190, China

Supporting Information

ABSTRACT: A wide variety of charge carrier dynamics, such as transport, separation, and extraction, occur at the interfaces of planar heterojunction solar cells. Such factors can affect the overall device performance. Therefore, understanding the buried interfacial molecular structure in various devices and the correlation between interfacial structure and function has become increasingly important. Current characterization techniques for thin films such as X-ray diffraction, cross section scanning electron microscopy, and UV–visible absorption spectroscopy are unable to provide the needed molecular structural information at buried interfaces. In this study, by controlling the structure of the hole transport layer (HTL) in a perovskite solar cell and applying a surface/interface-sensitive nonlinear vibrational spectroscopic technique (sum frequency generation vibrational spectroscopy (SFG)), we successfully probed the molecular structure at the buried interface and correlated its structural characteristics to solar cell performance. Here, an edge-on (normal to the interface) polythiophene (PT) interfacial molecular orientation at the buried perovskite (photoactive layer)/PT (HTL) interface showed more than two times the power conversion efficiency (PCE) of a lying down (tangential) PT interfacial orientation. The difference in interfacial molecular structure was achieved by altering the alkyl side chain length of the PT derivatives, where PT with a shorter alkyl side chain showed an edge-on interfacial orientation with a higher PCE than that of PT with a longer alkyl side chain. With similar band gap alignment and bulk structure within the PT layer, it is believed that the interfacial molecular structural variation (i.e., the orientation difference) of the various PT derivatives is the underlying cause of the difference in perovskite solar cell PCE.



INTRODUCTION

Perovskite, an organic–inorganic hybrid material, has shown exceptional performance in planar heterojunction solar cells. The power conversion efficiency (PCE) of perovskite solar cells has increased from 3.8% in 2009 to over 20% in 2014.^{1–3} A typical perovskite photoactive layer has an ABX₃ crystal structure, where A, B, and X are the organic cation, metal cation, and halide anion, respectively.³ Recent research has shown various approaches that can be adopted to improve properties of the perovskite photoactive layer. Such approaches have included varying the ABX₃ chemical composition to tune the band gap,^{3–6} using different solvent combinations to prepare the perovskite precursor to change the perovskite crystal structure during the annealing process,⁷ and adopting a rapid cooling rate after annealing to prepare a smooth and compact perovskite layer and minimize void formation.⁸ A typical planar heterojunction perovskite solar cell has a perovskite photoactive layer sandwiched between an electron transport layer (ETL) and a hole transport layer (HTL).^{2,3,5,9–17} By absorbing incoming photons, electrons

and holes are created inside the perovskite photoactive layer and extracted by the ETL and HTL, respectively.

For a perovskite solar cell with a highly crystallized, smooth, and compact photoactive layer, it is believed that device performance is determined by how efficiently charge carriers are transported and extracted across the interface by both the ETL and HTL. In an inverted structure perovskite solar cell, the ETL is typically a metal oxide (e.g., zinc oxide, titanium oxide, etc.), and the HTL is usually composed of organic molecules, such as Spiro-OMeTAD, benzodithiophene polymers (e.g., PTB7), or polythiophenes (e.g., P3HT).^{3,5,18–21} Some of these organic molecules have shown promising performance; the best PCE of solar cells made using these molecules ranges from 10% to 20%. It is relatively straightforward to analyze the structures of the ETL and perovskite photoactive layers due to their high crystallinity. However, structures of both the HTL bulk and the HTL

Received: October 11, 2016

Published: February 7, 2017

interface are not well-known and have remained under debate since the initial studies of organic photovoltaics (OPVs).^{22,23} Due to a lack of crystallinity, very few techniques can be used to provide insight or meaningful information about the HTL bulk structure. The bulk structure of an organic layer may be investigated by some X-ray-based techniques, e.g., X-ray absorption near edge spectroscopy (XANES), but such techniques can be quite complicated and are synchrotron-based. It is even more challenging to study the molecular structure of the HTL interface due to the lack of appropriate tools that can probe buried interfacial structures. It is believed that interfacial molecular orientation plays a vital role in charge transport, charge separation, and/or charge recombination; the interfacial structure is usually assumed using bulk X-ray diffraction results. Here, for the first time, we applied sum frequency generation (SFG) vibrational spectroscopy,²⁴ an interface-sensitive nonlinear optical spectroscopic technique, to investigate the buried interfacial structure between perovskite and the HTL.

SFG is a second-order nonlinear optical process where two photons are combined at an interface to generate a third photon that sums the energy of the two incoming photons. The selection rule of SFG dictates that this photon-combining process can only occur in a medium which lacks inversion symmetry. Most bulk media have inversion symmetry and cannot generate an SFG signal. For surfaces and interfaces, inversion symmetry is broken, and the SFG process can occur, allowing for SFG vibrational spectroscopy to be an intrinsic surface/interface-specific technique. In our SFG studies, the two incoming beams are visible (532 nm) and frequency-tunable infrared (IR) beams. By tuning the IR beam frequency, one can selectively probe various functional groups at an interface. Resolving the molecular orientation of such functional groups is achieved by controlling the polarization of each incoming beam as well as the generated SFG beam. Recent progress in SFG research has shown that SFG is a powerful tool to investigate surfaces and interfaces of many systems such as biological systems,^{25–30} organic molecules,^{31,32} and water surface/interfaces^{28,33–39} as well as organic semiconductor materials.^{40–46} The research reported in this article aims to understand the correlation between the structure of polythiophene (PT) at the buried perovskite/polythiophene (PT) interface in a solar cell and the solar cell efficiency.

This work focuses on a three-layer planar heterojunction perovskite solar cell. Titanium oxide serves as the ETL, and the HTL is made of PT derivatives. Solar cell samples with a similar structure were used for PCE measurements. Here, titanium oxide (ETL), perovskite, and PT (HTL) were sequentially deposited on top of an ITO-coated glass slide. UV–vis spectroscopy was used to study the band gaps of different PT derivatives. X-ray diffraction was used to characterize the crystallinity of perovskite and the alignment of the perovskite layer. X-ray diffraction and grazing incidence X-ray diffraction could also be used to study the bulk properties of the PT layer when the crystallinity of the PT layer was high. SFG was used to study the buried interface between PT and perovskite. Scanning electron microscopy (SEM) was used to study the surface morphology of the PT-coated perovskite surface. More details of the sample preparation and the experimental results will be presented below.

Numerous factors can affect the PCE of a solar cell.^{3–7,9,47,48} By systematically varying the side chain length of certain PT derivatives, we found that PT molecular orientations at the

buried interface were different. In addition, we found that using PT derivatives with different side chain lengths as the HTL material altered the PCE of the perovskite solar cell. We believe that the differences in PCE are related to the varied PT orientations at the interface.

MATERIALS AND METHODS

All PT derivatives (poly(3-hexylthiophene) (P3HT), poly(3-octylthiophene) (P3OT), poly(3-decylthiophene) (P3DT), poly(3-dodecylthiophene) (P3DDT)) were purchased from Rieke Metals (Lincoln, NE) and used as received. Methylammonium iodide (MAI) was ordered from Dyesol (Queanbeyan, Australia) and was also used as received. Lead chloride was purchased from Aldrich-Sigma (St. Louis, MO) and was used without further purification. The TiO₂ layer was synthesized via a sol–gel method.⁹ ITO glass substrates were sequentially washed with acetone, isopropanol, and distilled water (15 min each, assisted with ultrasonication). ITO glass was further cleaned by a 2 min glow discharge oxygen plasma. The TiO₂ sol–gel precursor was then spin-coated onto the ITO substrate at 2000 rpm for 1 min to prepare the TiO₂ ETL. The TiO₂ ETL on ITO glass was then annealed in air at 150 °C for 15 min, followed by 500 °C for 30 min. The perovskite precursor solution (278 mg PbCl₂ and 478 mg MAI dissolved in 1.7 g of DMF and mixed at 70 °C overnight before use) was then spin-coated onto the TiO₂ coated ITO glass at 2000 rpm for 60 s in a nitrogen-filled glovebox. After that, the spin-coated perovskite layer was annealed at 110 °C for 60 min. After cooling down, the PT derivatives (P3HT at 1.5 wt %, P3OT at 1.75 wt %, P3DT at 2.0 wt %, and P3DDT at 2.25 wt %) were spin-coated onto the perovskite layer at 1500 r.p.m for 45 s. Finally, the counter electrode was deposited by thermal evaporation of silver (100 nm) with a thermal evaporator at a pressure of 3×10^{-6} Torr.

Samples for SFG experiments were prepared in the same fashion but without silver deposition. To probe the buried interface using SFG, a layer of spin-coated poly(methyl methacrylate) (PMMA) (5 wt % in dichloromethane (DCM), spin-coated at 1500 r.p.m. for 1 min) was deposited on top of the PT layer prepared for SFG study. Different PT film thicknesses were achieved by varying the concentration of the PT solutions. SFG spectra were then collected from the perovskite/PT/PMMA layered samples using different polarizations of the input and output beams. SEM samples were prepared by spin-coating PTs onto the perovskite surfaces, and SEM images were obtained using a JEOL-7800FLV scanning electron microscope. Film thicknesses were measured by a depth profilometer (Dektak 6 M stylus Surface Profilometer, Veeco). The film thickness of a PT layer was deduced by taking the difference between the perovskite/PT film thickness and the pure perovskite film thickness.

PT derivatives spin-coated on quartz slides were used for UV–vis spectroscopy. Spectra were collected using a Shimadzu UV-1601 UV–vis spectrometer. Quartz slides were washed with acetone, isopropanol, Contrex, and distilled water (15 min each, assisted with ultrasonication), followed by a 1 min glow discharge oxygen plasma treatment.

Devices used for space charge limited current (SCLC) measurements were fabricated with an ITO/PT/Au structure, where the PT layer was spin-coated onto ITO glass with the same procedure as mentioned above. All SCLC measurements were performed in ambient air.

For transient photovoltage (TPV) measurements, a green LED was used as the light source along with a function generator as power supply. Decay of the voltage was monitored with an oscilloscope. All TPV measurements were performed using the devices fabricated with the previously described method.

The devices used for photoluminescence (PL) measurements were made with an ITO/TiO₂/perovskite/PT structure (as described previously) but without the silver electrode. All PL measurements were performed in ambient air.

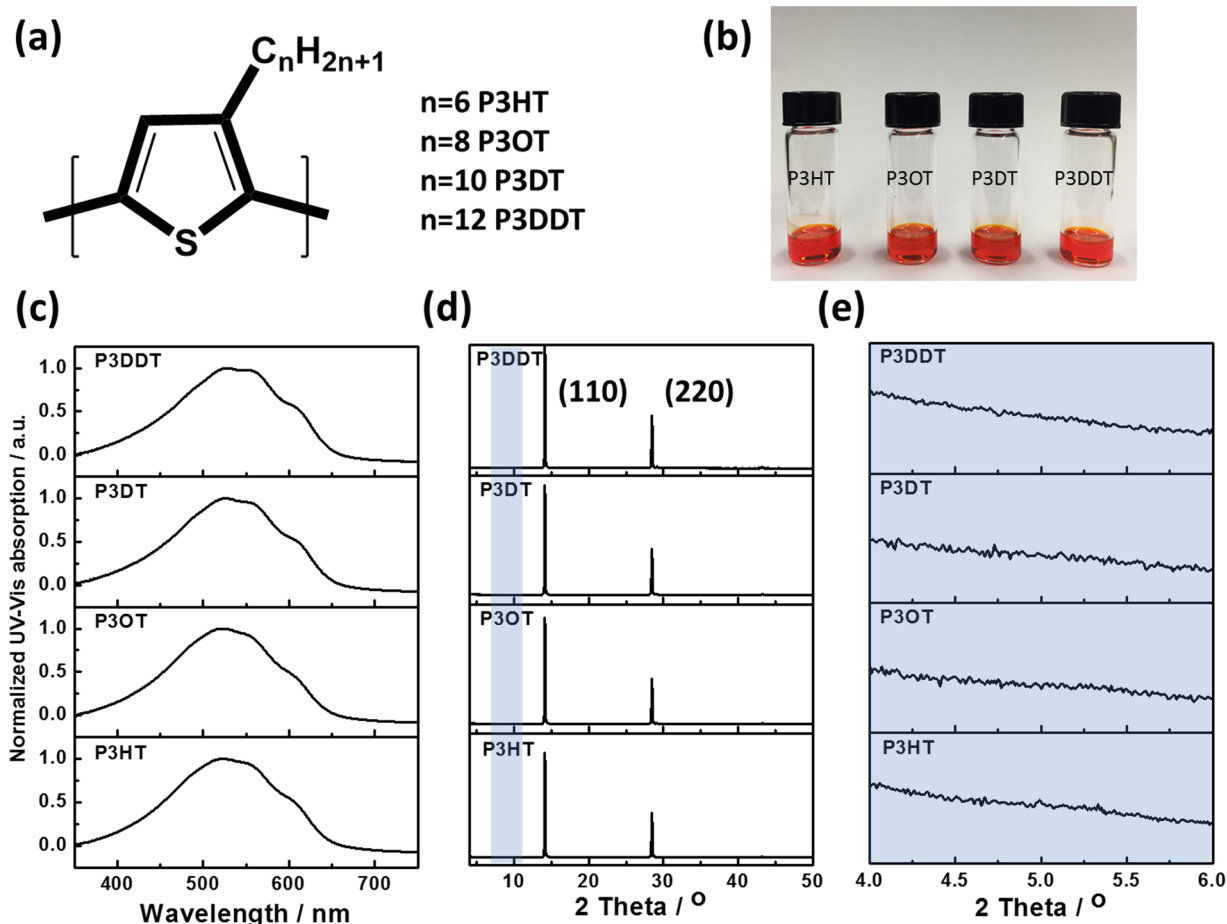


Figure 1. (a) Chemical formula of the PT derivatives used as the HTL material in this study. (b) PT derivatives dissolved in chlorobenzene show identical solution colors. (c) UV-vis spectra of spin-coated PT derivative thin films. (d) X-ray diffraction patterns of fabricated perovskite solar cells without silver electrodes. (e) Zoomed-in X-ray diffraction signals at 2θ ranging from 4.0° to 6.0° of the corresponding signals shown in (d).

SFG THEORY

Basic SFG theory, its selection rule, data interpretation, and molecular orientation calculation have been studied extensively,^{24,25,27,30,49,50} the details of which will not be repeated here. The SFG experimental setup used for this study was introduced previously^{31,40,51} and is briefly presented in the [Supporting Information](#). Here, we only present a method for SFG data analysis so that the results presented in later sections can be understood more easily. In SFG experiments, the SFG signal intensity is proportional to $\chi_{\text{eff}}^{(2)}$ and the intensities of the two input beams:

$$I_{\text{SFG}} \propto |\chi_{\text{eff}}^{(2)}|^2 I_{\text{IR}} I_{\text{vis}} \quad (1)$$

$\chi_{\text{eff}}^{(2)}$ is the effective second-order nonlinear optical susceptibility at the interface. Different $\chi_{\text{eff}}^{(2)}$ components can be measured through different polarization combinations of the input and signal beams (ssp: s-polarized signal beam, s-polarized visible input beam, and p-polarized input IR beam; and sps: s-polarized signal beam, p-polarized visible input beam, and s-polarized input IR beam), and we call them $\chi_{\text{eff,ssp}}^{(2)}$ and $\chi_{\text{eff,sps}}^{(2)}$ to name some examples. We then have

$$\chi_{\text{eff,ssp}}^{(2)} = L_{yy}(\omega) L_{yy}(\omega_1) L_{zz}(\omega_2) \sin \beta_2 \chi_{yyz} \quad (2)$$

$$\chi_{\text{eff,sps}}^{(2)} = L_{yy}(\omega) L_{zz}(\omega_1) L_{yy}(\omega_2) \sin \beta_1 \chi_{yzy} \quad (3)$$

where χ_{yyz} and χ_{yzy} are different components of $\chi^{(2)}$ within the laboratory-fixed coordinate, which is defined with the z-axis lying along the interface normal and x-axis in the input beam incident plane. L_{ii} (i = x, y, or z) is defined as the Fresnel coefficient, and β_1 and β_2 are

angles between the surface normal and the input visible/infrared beams, respectively.

Here, we aim to study the buried PT/perovskite interface. Samples prepared using a thin layer of PT spun onto a perovskite surface will generate SFG signal from multiple layers; contributions originate from both the PT/air surface and the PT/perovskite interface. Since the PT layer is thin, we are unable to separate the signals from the surface and the interface spatially. Unfortunately, we are unable to use a thick PT film because doing so would attenuate or block the IR beam. A polymer/air interface often generates a much stronger SFG signal than that from a buried interface, causing large errors for structural studies of the buried interface. Here, we deposited a thin layer of PMMA on top of the PT layer. This allows signals at the PMMA/PT interface (interface I) and the perovskite/PT interface (interface II) to have similar intensities. By varying the PT film thickness, we are able to modulate the interference of the SFG signals between interface I and interface II to separate the contribution of each. The detected SFG signal from the PT layer can be written as

$$\begin{aligned} \chi_{\text{eff,ssp}}^{(2)} = & L_{yy}^{\text{interfaceI}}(\omega) L_{yy}^{\text{interfaceI}}(\omega_1) L_{zz}^{\text{interfaceI}}(\omega_2) \sin \beta_2 \chi_{yyz}^{\text{interfaceI}} \\ & + L_{yy}^{\text{interfaceII}}(\omega) L_{yy}^{\text{interfaceII}}(\omega_1) L_{zz}^{\text{interfaceII}}(\omega_2) \sin \beta_2 \chi_{yyz}^{\text{interfaceII}} \\ & + \chi_{\text{NR}} e^{i\varphi_{\text{ssp}}} \end{aligned} \quad (4)$$

To simplify eq 4, Fresnel coefficients of different polarization combinations can be written as

$$F_{yyz}^{\text{interfaceI}} = |L_{yy}^{\text{interfaceI}}(\omega) L_{yy}^{\text{interfaceI}}(\omega_1) L_{zz}^{\text{interfaceI}}(\omega_2) \sin \beta_2| \quad (5)$$

$$F_{yyz}^{\text{interfacell}} = |L_{yy}^{\text{interfacell}}(\omega) L_{yy}^{\text{interfacell}}(\omega_1) L_{zz}^{\text{interfacell}}(\omega_2) \sin \beta_2| \quad (6)$$

Combining eqs 1 and 4–6, we have

$$I_{\text{SFG}} \propto C |F_{yyz}^{\text{interfacell}} \chi_{yyz}^{\text{interfacell}} e^{i\phi} + F_{yyz}^{\text{interfacell}} \chi_{yyz}^{\text{interfacell}} + \chi_{\text{NR}} e^{i\phi}|^2 \quad (7)$$

where Φ and ϕ are the phase difference between the SFG signals generated from interface I and interface II and the phase difference between the nonresonant background and interface II, respectively. The nonresonant background term can be obtained from SFG spectral fitting, and in this case, it is negligible. Previous studies have shown that SFG signal has a strong dependence on the interference of light caused by different thicknesses of the object film,^{51–54} and in this case, the Fresnel coefficients of different interfaces in the above equations can be calculated using a three-layer interference model.^{51,55–57} The Fresnel coefficients are also dependent on the PT film thickness (the thickness is embedded in the phase term of eq 7). To deconvolute $\chi_{yyz}^{\text{interfacell}}$ and $\chi_{yyz}^{\text{interfacell}}$ from the overall collected SFG signal intensity, we need two I_{SFG} measurements from films of two different thicknesses. Combining the measured SFG signals of the PT layers with two different thicknesses with calculated Fresnel coefficients of the two interfaces for each sample, we can deduce the $\chi_{yyz}^{\text{interfacell}}$ and $\chi_{yyz}^{\text{interfacell}}$ and furthermore reconstruct the SFG spectra originating from each layer, which will be shown in the presented results below. The film thicknesses of the PT layers in this study were carefully chosen to be 60 and 100 nm.^{51,53,56–58}

RESULTS AND DISCUSSION

As shown in Figure 1a, the PT derivatives used in this study differ only in their alkyl side chain length. Because the electric and optical properties of organic conjugated molecules rely heavily on their conjugated structure and conjugation length, altering the alkyl side chain length of the material used for the PT layer may not strongly affect such properties. Therefore, all PT derivatives utilized here should share a similar band structure. Figure 1b and c indicates similar optical properties of all the PT derivatives in the visible light frequency range. All PT derivatives showed an identical orange color in solution (Figure 1b). The measured UV–vis absorption of the PT thin films indicated a common major absorption peak at approximately 510 nm and a shoulder peak at approximately 600 nm (Figure 1c).^{48,59,60} The band gap of a PT derivative determines its hole-extracting nature at its contact with perovskite. Because of the similar absorption behavior in the visible range, the different PT derivatives utilized here are expected to have a similar band structure (the band diagram of P3HT (HTL), perovskite, and TiO₂ (ETL) is shown in Figure S1). Additionally, when different materials share similar band gap, mobility, and interfacial properties, their ability to extract holes is expected to be similar due to HOMO–HOMO alignment. A different band alignment can affect charge carrier transportation across the interface by changing open-circuit voltage, or it can even create a barrier to charge transport and therefore affect the overall PCE in a solar cell device. Here, because of the identical band gap alignment in all the PT derivatives studied, the band gap effect on PCE can be neglected. Information about the bulk structure of the PT derivatives may also be obtained from the UV–vis spectra. Since all four PT derivatives showed almost identical UV–vis spectral features, we believe that they should have similar bulk structures. Previous studies have shown controversial results about the correlation between side chain length and hole mobility for thiophene-based materials. Some stated that longer side chains lead to lower PT hole mobility,⁶¹ but others claimed that chain length does not appreciably affect mobility.⁶² We measured the hole mobilities of the PTs with

the shortest and longest side chain lengths, P3HT and P3DDT, via space charge limited current (SCLC) experiments using an ITO/PT/Au sandwiched structure. The results show that they have the same mobility, indicating that the mobility is independent of PT side chain length in our case (Figure S2).

Bulk structures of different materials will also affect the efficiency of charge carriers transported across these films and therefore have an impact on solar cell PCE. Figure 1d shows X-ray diffraction patterns of fabricated perovskite solar cells without silver electrodes. These X-ray diffraction patterns contain large contributions from the perovskite (110) plane.^{47,48,63} Figure 1e shows an enlarged section of Figure 1d with 2θ ranging from 4.0° to 6.0°. This range was chosen based on previously reported poly(3-hexylthiophene) (P3HT) X-ray diffraction patterns, where polycrystalline P3HT was shown to have an X-ray diffraction peak at approximately 5.2°.^{40,64–67} In this study, none of the PT derivatives showed any visible X-ray diffraction pattern on top of the perovskite surface, indicating the low crystallinity of the HTL prepared with all PT derivatives. Most organic semiconducting polymers are polycrystalline, but the observed X-ray diffraction patterns here showed that the PT films are mostly amorphous with a very low degree of crystallinity. In addition to powder X-ray diffraction, grazing incidence X-ray diffraction (GIXRD) was also used to study bulk structures within the PT. GIXRD is believed to have better sensitivity for thin film materials since X-rays propagate through the film. However, no visible peaks of any PT layers were observed (Figure S3 indicates GIXRD results). Both powder X-ray diffraction and GIXRD results suggested that the crystallinity inside the PT layer was low.

As presented in the Materials and Methods section, the UV–vis spectra discussed above were collected from PT films on quartz, not on perovskite. We could not collect UV–vis spectra from PT films on perovskite due to the broad absorption of perovskite. Clearly, the PT films on quartz have some crystallinity, and therefore, the absorption peak at 600 nm could be observed. We have previously studied the crystallinity of PT films on various substrates. Such studies demonstrated that PT films constructed on different substrate surfaces or prepared using different solvents indeed led to varied crystallinities.^{40,43} Here, the amorphous PT films are caused by the strong interactions with the perovskite surface. We therefore conclude that the PT polymers were mostly amorphous with a minimal degree of crystallinity in the solar cells in this study.

In addition to the bulk properties of the PT HTL, X-ray diffraction patterns can also be used to study perovskite thin film orientation. According to Figure 1d, the perovskite film has the (110) crystal plane in parallel to the film surface (defined as the x – y plane). Such an oriented perovskite structure can be further confirmed by comparing the data from the perovskite film to that from perovskite powder samples. The perovskite powder sample was prepared by scraping a perovskite thin film off the glass slide after annealing and grinding it into powder form; these data can be found in Figure S4. Various new peaks were observed in the X-ray diffraction pattern collected from the perovskite powder sample, indicating that for the powder sample, different crystal planes can be parallel to the x – y sample plane.

While the optical properties and bulk properties can be studied with UV–vis spectroscopy and X-ray diffraction, information regarding the interfacial molecular structure is still lacking. As reported above, the optical and bulk properties

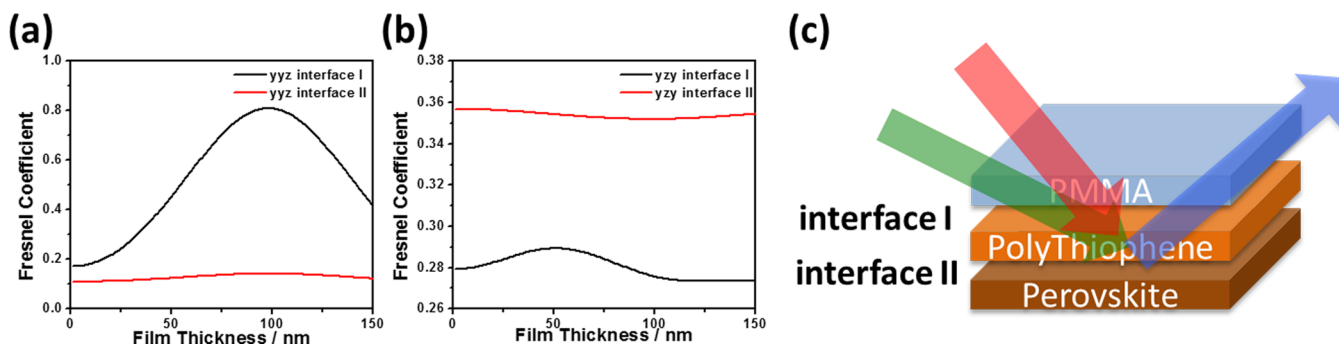


Figure 2. (a) Fresnel coefficient of the χ_{yz} component as a function of the PT layer film thickness (PMMA/PT/perovskite trilayer sample). (b) Fresnel coefficient of the χ_{zy} component as a function of PT layer film thickness (PMMA/PT/perovskite trilayer sample). (c) Illustration of interfaces I and II, as defined in the SFG experiment. All three layers are separated for clarity.

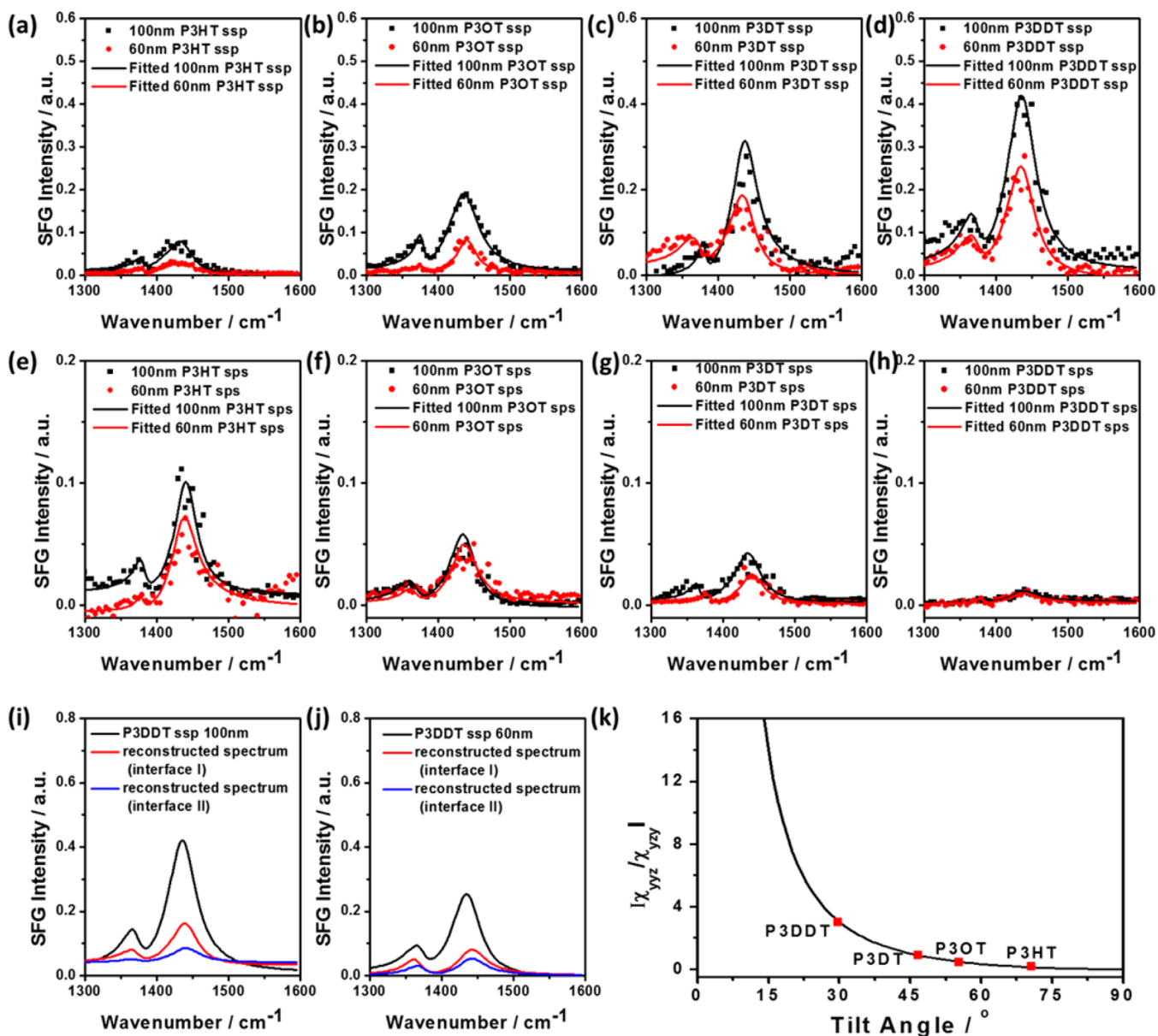


Figure 3. SFG ssp spectra collected from a PT thin film sandwiched between PMMA and perovskite: (a) P3HT, (b) P3OT, (c) P3DT, and (d) P3DDT. SFG sps spectra collected from the same samples: (e) P3HT, (f) P3OT, (g) P3DT, and (h) P3DDT. Reconstructed spectra including the overall spectrum and the spectra for interfaces I and II for P3DDT, ssp: (i) P3DDT film of 100 nm, (j) P3DDT film of 60 nm. (k) χ_{yz}/χ_{zy} ratio as a function of the tilt angle of the net transition dipole of the thiophene ring C=C stretch (with respect to the surface normal).

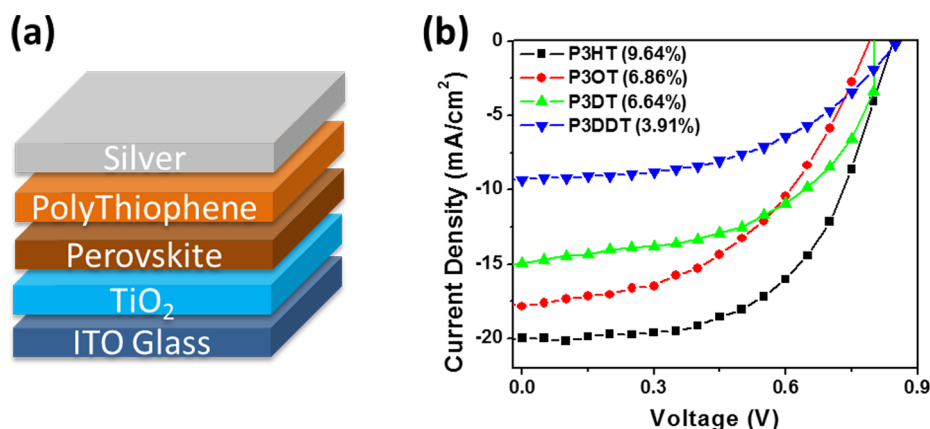


Figure 4. (a) Schematic showing the cross section of a fabricated perovskite solar cell. (b) J - V curves under AM 1.5 illumination of solar cell devices fabricated with various PT derivatives.

of different HTLs prepared with PT derivatives with different side chain lengths are nearly identical.

We then studied molecular structures of PT derivatives at the interface between the HTL and perovskite. As stated in the introduction, molecular orientation at buried interfaces can be deduced by the signals detected using sum frequency generation spectroscopy (SFG) with different polarization combinations of the input and signal photons. To facilitate analysis of the interfacial structures at the PT/perovskite interface, a PMMA capping layer was deposited on the PT layer. Dichloromethane (DCM), a poor solvent for P3HT, was chosen for casting PMMA in an effort to minimize any changes to the P3HT layer in a P3HT/PCBM bilayer organic solar cell.^{48,68} To confirm that DCM has minimal impact to the PT layer, SFG spectra collected from a P3HT layer before and after spin-coating with pure DCM can be found in the Supporting Information (Figure S5). The SFG spectrum of P3HT remains the same, demonstrating that DCM has no adverse effects on the PT surface structure.

With the PMMA capping layer, Fresnel coefficients of different $\chi^{(2)}$ components as a function of PT film thickness at both interface I (the PMMA/PT interface) and interface II (the PT/perovskite interface) are shown in Figure 2. Detected SFG signals from the layered structures shown in Figure 2c originated from both interfaces I and II. To extract the SFG response from only interface II (or the $\chi^{(2)}$ component of interface II), SFG spectra were collected from samples with at least two different PT film thicknesses. Thicknesses of 60 and 100 nm were chosen for study. Corresponding Fresnel coefficient values of both interfaces at the PT film thicknesses of 60 and 100 nm can be obtained from Figure 2 (χ_{ssp} probes χ_{yyz} , χ_{sps} probes χ_{yzy}). These values are used to deduce the value of $\chi^{(2)}$ from interface II.

Figure 3 shows SFG spectra of both ssp and sps polarizations collected from all PT derivatives. The peaks of interest are the C=C symmetric stretches in the thiophene five-membered ring at 1430 cm^{-1} ; such a symmetric five-membered thiophene ring has C_{2v} symmetry. It has been extensively reported that such a C=C symmetric stretch has a net transition dipole moment pointing perpendicular to the planar PT backbone. The smaller shoulder at 1375 cm^{-1} is the C-C ν_s (ring) stretch, and both peaks are consistent with previous studies.^{41,69,70} We fitted these SFG spectra, with the detailed peak fitting results listed in the Supporting Information (Table S1). It is worth mentioning that the SFG spectra have contributions from both

interfaces I and II. Using the Fresnel coefficients of each interface, we are able to deduce the χ_{yyz} and χ_{yzy} components for each individual interface. Here, we are more interested in the interface between PT and perovskite: interface II. Using the fitted data listed in Table S1, we can calculate the ratio of $\chi_{\text{yyz}}/\chi_{\text{yzy}}$ for interface II, from which we can deduce the orientation of the PT at that interface. Figure 3k shows the correlation between the deduced $\chi_{\text{yyz}}/\chi_{\text{yzy}}$ value and the PT backbone orientation.

Interestingly, the measured $\chi_{\text{yyz}}/\chi_{\text{yzy}}$ ratio showed an increasing trend with increasing length of the PT alkyl side chain. The smallest $\chi_{\text{yyz}}/\chi_{\text{yzy}}$ measured was 0.36 with P3HT, while the largest $\chi_{\text{yyz}}/\chi_{\text{yzy}}$ was 3.72 with P3DDT. Using these experimentally measured $\chi_{\text{yyz}}/\chi_{\text{yzy}}$ values and their correlations with the tilt angle of the PT backbone, plotted in Figure 3k, we can determine the backbone orientations of PT molecules at the buried PT/perovskite interface. The P3HT polythiophene backbone orientation was deduced to be approximately 20° with respect to the surface normal, increasing to approximately 60° for P3DDT. From these results, we are able to conclude that the thiophene backbone of P3HT adopts a more normal (upright) orientation on the perovskite (110) crystal plane, and P3DDT's thiophene backbone lies more tangentially (flat). The angles of P3OT and P3DT lie in between those of P3HT and P3DDT. Therefore, for PT molecules on the perovskite (110) plane, in all four PT derivatives examined here, a shorter alkyl side chain results in a more upright orientation of the PT backbone.

It has been shown extensively that surface or interfacial molecules can have preferred orientations due to the disruption of inversion symmetry at the surface/interface, where specific interactions exist.⁷¹ For example, many surface/interfacial functional groups of amorphous polymers exhibit preferred orientations, and such orientations can be varied at different interfaces due to interfacial interactions.⁷¹ We also showed that because of such interfacial interactions, polythiophene molecules exhibit varied orientations when in contact with different surfaces and with different side chains.^{40,43} Here, PTs have different side chains, which led to strong or weak interactions with perovskite, resulting in varied PT backbone orientations while in contact with perovskite.

We have not investigated the behavior of the PT side chain at the buried PT/perovskite interface, because perovskite methyl groups may also contribute to the C-H stretching signals, which will overlap with the side chain SFG signal. Here, it is

more important to study the thiophene backbone because in organic semiconductors, only the conjugated system is responsible for charge carrier extraction and transportation. We believe that this thiophene backbone will be the dominant factor for the entire hole extraction process across the PT/perovskite interface.

The surface morphologies of perovskite solar cells with various PT derivatives detected by SEM can be found in Figure S6. All perovskite/PT surfaces showed good homogeneity, with a visible perovskite crystalline domain. A rigid and homogeneous perovskite surface is usually the key for high-performance perovskite solar cells, as reported previously.^{3,8} The perovskite crystalline domain remains visible after each PT layer coating, and surface morphology does not depend on the PT side chain length.

After we characterized the optical properties of the HTL on perovskite using UV–vis spectroscopy, the bulk structure and crystallinity using X-ray diffraction, the surface morphology using SEM, and the interface structure using SFG, we fabricated perovskite solar cell devices with the structure shown in Figure 4 to test how various PT derivatives would affect overall device PCE. Detailed fabrication methods were reported in the Materials and Methods section. Figure 4 shows the PCE from the champion cell made with each PT derivative. All PT derivatives showed almost identical V_{oc} of approximately 0.8 V, with FF factors calculated at or above 50% (detailed V_{oc} , J_{sc} , and FF values are listed in Table 1). While the band gap difference

Table 1. Photovoltaic Performance of Perovskite Solar Cells Fabricated with Different HTL Materials

HTL material	V_{oc} (V)	J_{sc} (mA/mc ²)	FF	PCE (%)
P3HT	0.82	19.97	58.88%	9.64
P3OT	0.79	17.84	48.66%	6.86
P3DT	0.83	14.96	53.43%	6.64
P3DDT	0.85	9.31	49.44%	3.91

between the HTL (ETL) and the photoactive layer is believed to dominate V_{oc} in a solar cell, the above result proves the same band gap alignment for different solar cells made using different PTs as reported in Figure S1. Interestingly, solar cells made using different PTs have varied J_{sc} values. P3HT, with the most upright orientation, has a J_{sc} of 21.22 mA, while P3DDT, with the most lying down orientation, has a J_{sc} of 9.3 mA.

For a photovoltaic device, the interface between the perovskite layer and HTL is where holes are extracted. Solar cells prepared with different PT derivatives having different side chains in this study contain identical ETL and perovskite layers. The different PT orientations at the interface in these solar cells affect the hole transport process. Because holes are transported through HOMOs, the relative orientation between the HOMOs of PT and perovskite as a result of different PT orientations becomes the key for solar cell performance. According to previously studied HOMOs of both P3HT and lead iodine-based perovskite,^{72,73} they would overlap better with a lying down PT thiophene backbone orientation. Therefore, an edge-on thiophene backbone would lead to a greater offset of HOMO–HOMO between perovskite and PTs. Our experimental data obtained above show that the solar cell made of PT with a more normal (edge-on or standing up) thiophene backbone orientation at the interface has a 2 times higher J_{sc} than that made of PT with a more tangential (lying down) thiophene backbone. We therefore believe that an offset

HOMO–HOMO alignment between the perovskite and HTL is better for hole extraction at such an interface, while a more overlapped HOMO–HOMO between perovskite and HTL would possibly lead to more electron–hole recombination at the interface, meaning that hole extraction at the perovskite/HTL interface is far less efficient.

To better understand the charge carrier lifetime and trap density, transient photovoltage (TPV) and transient photocurrent (TPC) experiments were performed on devices fabricated with P3HT and P3DDT, respectively (Figure S7). As the TPV results show, the device fabricated with P3HT has a longer charge carrier lifetime than does that fabricated with P3DDT. The TPC result shows a longer decay for the device fabricated with P3DDT compared to that of P3HT, indicating a high density of trapping states in the device fabricated with P3DDT. Because the TPC experiment was performed on an entire photovoltaic device, it is difficult to distinguish the trap at the perovskite/PT interface from the trap in the PT layer (bulk). If the trapping state at the interface plays a role in hole extraction, the orientation of the PT backbone may also have a direct correlation with the abundance of the trapping state.^{3,74–77}

We also performed a PL quenching study on both perovskite/P3HT and perovskite/P3DDT samples. Our results clearly show that the device made with P3DDT exhibits a stronger PL response compared to that with P3HT (Figure S8) and indicate that P3HT extracts holes more efficiently than P3DDT. Because hole extraction only occurs at the interface, such a finding is consistent with our proposed mechanism.

Previous studies have investigated interfacial structures in photovoltaic applications. For example, Ayzner et al. proposed that a varied LUMO–LUMO offset between CuPc and C₆₀ can change the electron transfer rate up to four times.²² A similar claim was made by Rand et al.²³ Combined with these results, our data above indicate that the electron orbital alignment at the interface plays the key role in device performance. Such electron orbital alignment is determined by the interfacial molecular orientation. This is why interfacial molecular orientation is crucial to photovoltaic device performance.

CONCLUSION

We have investigated the interfacial orientations of PT molecules with different side chain lengths at the PT/perovskite buried interface and their correlation with the performance of perovskite photovoltaic devices. In addition to the interfacial structure, the optical properties, bulk structures, and surface morphologies of the PT layers were also studied. Interestingly, all PT derivatives with different side chain lengths showed identical UV–vis absorption spectra in the wavelength range of 350 nm–750 nm, demonstrating similar band structure of all PT derivatives. No signals could be detected from these PT layers using XRD and GIXRD, indicating that such PT materials have a dominant amorphous structure in bulk (or exhibit very low crystallinity).

Our SFG studies showed that the orientation of the PT thiophene backbone at the buried PT/perovskite interface depended on the alkyl side chain length (Figure 5). PCE measurements indicated that the performance of perovskite solar cells varied with PT side chain length. Therefore, we believe that the orientation of the PT thiophene backbone at the perovskite interface is correlated to perovskite solar cell performance. It was found that normal (standing up) and tangential (lying down) thiophene backbone orientations led to

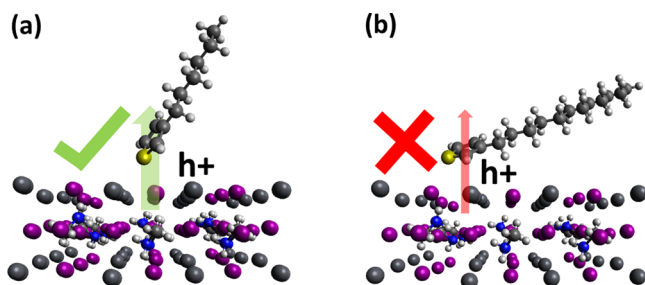


Figure 5. Illustration of hole extraction ability of (a) PTs with shorter alkyl side chain and (b) PTs with longer alkyl side chain at the HTL/perovskite interface.

different J_{sc} values (up to a two times difference) while keeping V_{oc} similar. V_{oc} of a solar cell is determined primarily by the band gap energy difference, so the similar V_{oc} values measured in this study further validate the similar band structures of different PTs. The J_{sc} result of more than a two times difference between the longest and shortest polythiophene side chains (P3HT, 20.0 mA/cm²; P3DDT, 9.3 mA/cm²) shows a strong correlation of the hole extraction efficiency and the PT backbone orientation at the HTL/perovskite interface. Our data indicated that a more normal orientation of the HTL backbone at the HTL/perovskite interface is better for hole extraction efficiency. Here, we demonstrated that an offset HOMO–HOMO alignment between the perovskite and HTL (determined by the interfacial PT backbone orientation) is better for hole extraction at the PT/perovskite interface. Therefore, the orientation of the PT backbone at the buried perovskite/HTL interface plays an important role in determining solar cell efficiency. We believe that this conclusion can be applied to different perovskite solar cell systems using different HTL materials including Spiro-OMeTAD. That is, the interfacial orientation of the ring structure of Spiro-OMeTAD at the perovskite/Spiro-OMeTAD interface likely would impact the solar cell efficiency, which will be investigated in detail in the future.

We believe that this is the first study to correlate the buried interfacial structure in a perovskite solar cell to its performance. It was found that the interfacial molecular orientation influences solar cell PCE. If the interfacial orientation of the thiophene backbone could be more perpendicular to the interface, the solar cell performance should be improved. We believe that, in the future, rational design of the buried interface in solar cells will result in improvements to performance. This research again demonstrates the power of SFG to probe buried interfaces. While for solar cell research, this study only studied the HTL/photoactive layer interface of perovskite solar cells, it is believed and already demonstrated to some extent that other interfaces such as photoactive/ETL, donor/acceptor, etc. in different photovoltaic materials and structures will also have a strong impact on charge carrier dynamics across the interface. It is feasible to apply SFG to understand the structural and functional relations of these interfaces in photovoltaic devices. Such knowledge will have broader impacts on the research field of photovoltaics in the future.

■ ASSOCIATED CONTENT

📄 Supporting Information

The Supporting Information is available free of charge on the ACS Publications website at DOI: 10.1021/jacs.6b10651.

Introduction of SFG setup, P3HT surface spectrum before and after spin-coating with pure DCM, detailed peak fitting parameters, and results from PL quenching, OPV, and SCLC experiments (PDF)

■ AUTHOR INFORMATION

Corresponding Authors

*guo@umich.edu

*zhanc@umich.edu

ORCID

Minyu Xiao: 0000-0003-0083-4243

Jialiu Ma: 0000-0002-5481-9383

Notes

The authors declare no competing financial interest.

■ ACKNOWLEDGMENTS

This research is supported by the University of Michigan. X.Z. thanks the National Nature Science Foundation of China (Grant 11604064) for their financial support.

■ REFERENCES

- (1) Kojima, A.; Teshima, K.; Shirai, Y.; Miyasaka, T. *J. Am. Chem. Soc.* **2009**, *131*, 6050–6051.
- (2) Snaith, H. J. *J. Phys. Chem. Lett.* **2013**, *4*, 3623–3630.
- (3) Zhou, H.; Chen, Q.; Li, G.; Luo, S.; Song, T.-b.; Duan, H.-S.; Hong, Z.; You, J.; Liu, Y.; Yang, Y. *Science* **2014**, *345*, 542–546.
- (4) Abrusci, A.; Stranks, S. D.; Docampo, P.; Yip, H.-L.; Jen, A. K.-Y.; Snaith, H. J. *Nano Lett.* **2013**, *13*, 3124–3128.
- (5) Conings, B.; Baeten, L.; De Dobbelaere, C.; D’Haen, J.; Manca, J.; Boyen, H. G. *Adv. Mater.* **2014**, *26*, 2041–2046.
- (6) Meng, L.; You, J.; Guo, T.-F.; Yang, Y. *Acc. Chem. Res.* **2016**, *49*, 155–165.
- (7) Jeon, N. J.; Noh, J. H.; Kim, Y. C.; Yang, W. S.; Ryu, S.; Seok, S. I. *Nat. Mater.* **2014**, *13*, 897–903.
- (8) Guo, Y.; Liu, C.; Inoue, K.; Harano, K.; Tanaka, H.; Nakamura, E. *J. Mater. Chem. A* **2014**, *2*, 13827–13830.
- (9) Docampo, P.; Ball, J. M.; Darwich, M.; Eperon, G. E.; Snaith, H. J. *Nat. Commun.* **2013**, *4*, 2761.
- (10) Lee, M. M.; Teuscher, J.; Miyasaka, T.; Murakami, T. N.; Snaith, H. J. *Science* **2012**, *338*, 643–647.
- (11) Liu, M.; Johnston, M. B.; Snaith, H. J. *Nature* **2013**, *501*, 395–398.
- (12) Xing, Y.; Sun, C.; Yip, H.-L.; Bazan, G. C.; Huang, F.; Cao, Y. *Nano Energy* **2016**, *26*, 7–15.
- (13) Bai, Y.; Chen, H.; Xiao, S.; Xue, Q.; Zhang, T.; Zhu, Z.; Li, Q.; Hu, C.; Yang, Y.; Hu, Z.; et al. *Adv. Funct. Mater.* **2016**, *26*, 2950–2958.
- (14) Liao, W.; Zhao, D.; Yu, Y.; Grice, C. R.; Wang, C.; Cimaroli, A. J.; Schulz, P.; Meng, W.; Zhu, K.; Xiong, R. G.; Yan, Y. *Adv. Mater.* **2016**, *28*, 9333–9340.
- (15) Liao, W.; Zhao, D.; Yu, Y.; Shrestha, N.; Ghimire, K.; Grice, C. R.; Wang, C.; Xiao, Y.; Cimaroli, A.; Ellingson, R. J.; et al. *J. Am. Chem. Soc.* **2016**, *138*, 12360–12363.
- (16) Cha, M.; Da, P.; Wang, J.; Wang, W.; Chen, Z.; Xiu, F.; Zheng, G.; Wang, Z.-S. *J. Am. Chem. Soc.* **2016**, *138*, 8581–8587.
- (17) Chen, S.; Lei, L.; Yang, S.; Liu, Y.; Wang, Z.-S. *ACS Appl. Mater. Interfaces* **2015**, *7*, 25770–25776.
- (18) Kim, J.; Kim, G.; Kim, T. K.; Kwon, S.; Back, H.; Lee, J.; Lee, S. H.; Kang, H.; Lee, K. *J. Mater. Chem. A* **2014**, *2*, 17291–17296.
- (19) Hsiao, Y.-S.; Charan, S.; Wu, F.-Y.; Chien, F.-C.; Chu, C.-W.; Chen, P.; Chen, F.-C. *J. Phys. Chem. C* **2012**, *116*, 20731–20737.
- (20) Huang, J.-H.; Yang, C.-Y.; Ho, Z.-Y.; Kekuda, D.; Wu, M.-C.; Chien, F.-C.; Chen, P.; Chu, C.-W.; Ho, K.-C. *Org. Electron.* **2009**, *10*, 27–33.
- (21) Wu, J.-L.; Chen, F.-C.; Hsiao, Y.-S.; Chien, F.-C.; Chen, P.; Kuo, C.-H.; Huang, M. H.; Hsu, C.-S. *ACS Nano* **2011**, *5*, 959–967.

- (22) Ayzner, A. L.; Nordlund, D.; Kim, D.-H.; Bao, Z.; Toney, M. F. *J. Phys. Chem. Lett.* **2015**, *6*, 6–12.
- (23) Rand, B. P.; Cheyens, D.; Vasseur, K.; Giebink, N. C.; Mothy, S.; Yi, Y.; Coropceanu, V.; Beljonne, D.; Cornil, J.; Brédas, J. L.; Genoe, J. *Adv. Funct. Mater.* **2012**, *22*, 2987–2995.
- (24) Shen, Y. *Nature* **1989**, *337*, 519–525.
- (25) Li, Y.; Zhang, X.; Myers, J.; Abbott, N. L.; Chen, Z. *Chem. Commun.* **2015**, *51*, 11015–11018.
- (26) Li, Y.; Wei, S.; Wu, J.; Jasensky, J.; Xi, C.; Li, H.; Xu, Y.; Wang, Q.; Marsh, E. N. G.; Brooks, C. L., III; Chen, Z. *J. Phys. Chem. C* **2015**, *119*, 7146–7155.
- (27) Wang, J.; Even, M. A.; Chen, X.; Schmaier, A. H.; Waite, J. H.; Chen, Z. *J. Am. Chem. Soc.* **2003**, *125*, 9914–9915.
- (28) Okuno, M.; Ishibashi, T.-a. *J. Phys. Chem. C* **2015**, *119*, 9947–9954.
- (29) Ho, J.-J.; Skoff, D. R.; Ghosh, A.; Zanni, M. T. *J. Phys. Chem. B* **2015**, *119*, 10586–10596.
- (30) Ding, B.; Jasensky, J.; Li, Y.; Chen, Z. *Acc. Chem. Res.* **2016**, *49*, 1149–1157.
- (31) Leng, C.; Hung, H.-C.; Sieggreen, O. A.; Li, Y.; Jiang, S.; Chen, Z. *J. Phys. Chem. C* **2015**, *119*, 8775–8780.
- (32) Hu, D.; Chou, K. C. *J. Am. Chem. Soc.* **2014**, *136*, 15114–15117.
- (33) Hsieh, C. S.; Okuno, M.; Hunger, J.; Backus, E. H.; Nagata, Y.; Bonn, M. *Angew. Chem., Int. Ed.* **2014**, *53*, 8146–8149.
- (34) van der Post, S. T.; Hsieh, C.-S.; Okuno, M.; Nagata, Y.; Bakker, H. J.; Bonn, M.; Hunger, J. *Nat. Commun.* **2015**, *6*, 8384.
- (35) Lis, D.; Backus, E. H.; Hunger, J.; Parekh, S. H.; Bonn, M. *Science* **2014**, *344*, 1138–1142.
- (36) Zhang, Y.; Furyk, S.; Bergbreiter, D. E.; Cremer, P. S. *J. Am. Chem. Soc.* **2005**, *127*, 14505–14510.
- (37) Anim-Danso, E.; Zhang, Y.; Dhinojwala, A. *J. Am. Chem. Soc.* **2013**, *135*, 8496–8499.
- (38) Sagle, L. B.; Cimat, K.; Litosh, V. A.; Liu, Y.; Flores, S. C.; Chen, X.; Yu, B.; Cremer, P. S. *J. Am. Chem. Soc.* **2011**, *133*, 18707–18712.
- (39) Zhang, Y.; Cremer, P. S. *Curr. Opin. Chem. Biol.* **2006**, *10*, 658–663.
- (40) Xiao, M.; Zhang, X.; Bryan, Z. J.; Jasensky, J.; McNeil, A. J.; Chen, Z. *Langmuir* **2015**, *31*, 5050–5056.
- (41) Anglin, T. C.; Speros, J. C.; Massari, A. M. *J. Phys. Chem. C* **2011**, *115*, 16027–16036.
- (42) Sohrabpour, Z.; Kearns, P. M.; Massari, A. M. *J. Phys. Chem. C* **2016**, *120*, 1666–1672.
- (43) Xiao, M.; Jasensky, J.; Zhang, X.; Li, Y.; Pichan, C.; Lu, X.; Chen, Z. *Phys. Chem. Chem. Phys.* **2016**, *18*, 22089–22099.
- (44) Ye, H.; Abu-Akeel, A.; Huang, J.; Katz, H. E.; Gracias, D. H. *J. Am. Chem. Soc.* **2006**, *128*, 6528–6529.
- (45) Dhar, P.; Khlyabich, P. P.; Burkhart, B.; Roberts, S. T.; Malyk, S.; Thompson, B. C.; Benderskii, A. V. *J. Phys. Chem. C* **2013**, *117*, 15213–15220.
- (46) Walter, S. R.; Youn, J.; Emery, J. D.; Kewalramani, S.; Hennek, J. W.; Bedzyk, M. J.; Facchetti, A.; Marks, T. J.; Geiger, F. M. *J. Am. Chem. Soc.* **2012**, *134*, 11726–11733.
- (47) Erb, T.; Zhokhavets, U.; Gobsch, G.; Raleva, S.; Stühn, B.; Schilinsky, P.; Waldauf, C.; Brabec, C. *J. Adv. Funct. Mater.* **2005**, *15*, 1193–1196.
- (48) Vanlaeke, P.; Swinnen, A.; Haeldermans, I.; Vanhoyland, G.; Aernouts, T.; Cheyens, D.; Deibel, C.; D’Haen, J.; Heremans, P.; Poortmans, J.; Manca, J. V. *Sol. Energy Mater. Sol. Cells* **2006**, *90*, 2150–2158.
- (49) Chen, Z.; Shen, Y.; Somorjai, G. A. *Annu. Rev. Phys. Chem.* **2002**, *53*, 437–465.
- (50) Wang, J.; Paszti, Z.; Even, M. A.; Chen, Z. *J. Am. Chem. Soc.* **2002**, *124*, 7016–7023.
- (51) Myers, J. N.; Zhang, X.; Bielefeld, J.; Lin, Q.; Chen, Z. *J. Phys. Chem. B* **2015**, *119*, 1736–1746.
- (52) FitzGerald, W. R.; Jena, K. C.; Hore, D. K. *J. Mol. Struct.* **2015**, *1084*, 368–373.
- (53) Kearns, P. M.; O’Brien, D. B.; Massari, A. M. *J. Phys. Chem. Lett.* **2016**, *7*, 62–68.
- (54) Zhang, X.; Myers, J. N.; Huang, H.; Shobha, H.; Chen, Z.; Grill, A. *J. Appl. Phys.* **2016**, *119*, 084101.
- (55) Lu, X.; Clarke, M. L.; Li, D.; Wang, X.; Xue, G.; Chen, Z. *J. Phys. Chem. C* **2011**, *115*, 13759–13767.
- (56) Lu, X.; Li, D.; Kristalyn, C. B.; Han, J.; Shephard, N.; Rhodes, S.; Xue, G.; Chen, Z. *Macromolecules* **2009**, *42*, 9052–9057.
- (57) Lu, X.; Shephard, N.; Han, J.; Xue, G.; Chen, Z. *Macromolecules* **2008**, *41*, 8770–8777.
- (58) Wang, T.; Li, D.; Lu, X.; Khmaladze, A.; Han, X.; Ye, S.; Yang, P.; Xue, G.; He, N.; Chen, Z. *J. Phys. Chem. C* **2011**, *115*, 7613–7620.
- (59) Winokur, M.; Spiegel, D.; Kim, Y.; Hotta, S.; Heeger, A. *Synth. Met.* **1989**, *28*, 419–426.
- (60) Anglin, T. C.; Lane, A. P.; Massari, A. M. *J. Mater. Chem. C* **2014**, *2*, 3390–3400.
- (61) Cho, C.-H.; Kim, H. J.; Kang, H.; Shin, T. J.; Kim, B. J. *J. Mater. Chem.* **2012**, *22*, 14236–14245.
- (62) Oosterbaan, W. D.; Bolsée, J. C.; Gadisa, A.; Vrindts, V.; Bertho, S.; D’Haen, J.; Cleij, T. J.; Lutsen, L.; McNeill, C. R.; Thomsen, L.; et al. *Adv. Funct. Mater.* **2010**, *20*, 792–802.
- (63) Ma, W.; Yang, C.; Gong, X.; Lee, K.; Heeger, A. J. *Adv. Funct. Mater.* **2005**, *15*, 1617–1622.
- (64) Brinkmann, M.; Rannou, P. *Adv. Funct. Mater.* **2007**, *17*, 101–108.
- (65) Kim, D. J.; Jang, Y.; Yang, H.; Kim, Y. H.; Han, J. I.; Moon, D. G.; Park, S.; Chang, T.; Chang, C.; Joo, M. *Adv. Funct. Mater.* **2005**, *15*, 77–82.
- (66) Dudenko, D.; Kiersnowski, A.; Shu, J.; Pisula, W.; Sebastiani, D.; Spiess, H. W.; Hansen, M. R. *Angew. Chem., Int. Ed.* **2012**, *51*, 11068–11072.
- (67) Yamamoto, K.; Ochiai, S.; Wang, X.; Uchida, Y.; Kojima, K.; Ohashi, A.; Mizutani, T. *Thin Solid Films* **2008**, *516*, 2695–2699.
- (68) Lee, K. H.; Schwenn, P. E.; Smith, A. R.; Cavaye, H.; Shaw, P. E.; James, M.; Krueger, K. B.; Gentle, I. R.; Meredith, P.; Burn, P. L. *Adv. Mater.* **2011**, *23*, 766–770.
- (69) Yun, J.-J.; Peet, J.; Cho, N.-S.; Bazan, G. C.; Lee, S. J.; Moskovits, M. *Appl. Phys. Lett.* **2008**, *92*, 251912.
- (70) Gao, Y.; Grey, J. K. *J. Am. Chem. Soc.* **2009**, *131*, 9654–9662.
- (71) Chen, Z. *Prog. Polym. Sci.* **2010**, *35*, 1376–1402.
- (72) Prajontat, P.; Wargulski, D. R.; Unold, T.; Dittrich, T. *J. Phys. Chem. C* **2016**, *120*, 3876–3881.
- (73) Wong, F.; Perez, G.; Bonilla, M.; Colon-Santana, J. A.; Zhang, X.; Sharma, P.; Gruverman, A.; Dowben, P. A.; Rosa, L. G. *RSC Adv.* **2014**, *4*, 3020–3027.
- (74) Li, Z.; Gao, F.; Greenham, N. C.; McNeill, C. R. *Adv. Funct. Mater.* **2011**, *21*, 1419–1431.
- (75) Li, Z.; Lakhwani, G.; Greenham, N. C.; McNeill, C. R. *J. Appl. Phys.* **2013**, *114*, 034502.
- (76) McNeill, C. R.; Hwang, I.; Greenham, N. C. *J. Appl. Phys.* **2009**, *106*, 024507.
- (77) Xiao, Z.; Dong, Q.; Bi, C.; Shao, Y.; Yuan, Y.; Huang, J. *Adv. Mater.* **2014**, *26*, 6503–6509.